An incompressible multi-phase SPH method

X. Y. Hu and N. A. Adams

Lehrstuhl für Aerodynamik, Technische Universität München
85748 Garching, Germany

Abstract

An incompressible multi-phase SPH method is proposed. In this method, a fractional time-step method is introduced to enforce both the zero-density-variation condition and the velocity-divergence-free condition at each full time step. To obtain sharp density and viscosity discontinuities in an incompressible multi-phase flow a new multi-phase projection formulation, in which the discretized gradient and divergence operators do not require a differentiable density or viscosity field is proposed. Numerical examples for Taylor-Green flow, capillary waves, drop deformation in shear flows and for Rayleigh-Taylor instability are presented and compared to theoretical solutions or references from literature. The results suggest good accuracy and convergence properties of the proposed method.

Key words: multi-phase flows, incompressible flow, particle method

1 Introduction

The smoothed particle hydrodynamics (SPH) method is a fully Lagrangian, grid free method in which a smoothing kernel is introduced to approximate functions and their spatial derivatives originating from the interactions with neighboring particles. Since its introduction by Lucy [**?**] and Gingold & Monaghan [**?**], SPH has been applied to a wide range of flow problems [**?**] [**?**]. The original formulation of SPH is for compressible flows and permits the evolution of fluid densities along flow trajectories. When SPH is applied to simulate incompressible flows, there are generally two ways to impose incompressibility: one is the weakly compressible SPH formulation [**?**][**?**][**?**] [**?**][**?**][**?**] which approximates incompressibility by assuming a small Mach number, usually $M \leq 0.1$; the other is the incompressible SPH in which incompressibility is enforced by solving a Poisson equation with a source term proportional to the velocity divergence [**?**] or the density variation [**?**]. Compared with weakly compressible SPH the latter gives more accurate solutions and is computationally more efficient for flow phenomena at moderate to high Reynolds numbers.

In an ideal incompressible SPH computation particles should adjust their positions to an uniform distribution so that their density variation vanishes. If only a discrete velocity-divergence-free condition is enforced larger density variation or particle clustering may occur due to the spatial truncation error of the discretization scheme. Furthermore, the density errors can accumulate during long time computations [**?**]. Pozorski & Wawreńczuk [**?**] suggested to solve simultaneously the Poisson equations related to density variation and related to velocity divergence. However, their method does not solve the difficulties concerning particle clustering and density-error accumulation. Ellero et al. [**?**] introduce the SHAKE algorithm of molecular dynamics to constrain the density variation. While correcting the density error by modifying particle position iteratively, their method produces relatively larger particle clustering than that of the weakly compressible SPH.

For multi-phase flows the interface represented by SPH is usually strongly smeared since both the divergence and gradient operators are commonly formulated stipulating a differentiable density field with a gradient much smaller than that of the smoothing kernel [**?**] [**?**]. Hu & Adams [**?**] have proposed a new particle-averaged spatial derivative approximation to handle density and viscosity discontinuities directly without smearing. Since there is no transition region with large density gradient, no spurious pressure (artificial surface tension) is introduced [**?**]. This method, however, is based on a weakly compressible SPH formulation which in practice is limited to small Reynolds numbers or meso-scopic flows.

In this paper, a technique for a multi-phase SPH by enforcing simultaneously constraints on density variation and on velocity is developed. The essential steps are that first the intermediate particle velocities are computed at the intermediate half time step and at the full time step, respectively, and that an intermediate particle position at the full time-step is obtained from the previous time step without enforcing any constraint. In a second step the intermediate particle position at the full time step is modified iteratively to satisfy the zero-density-variation condition. At these new particle positions, the intermediate particle velocity at the full time step is modified by enforcing the velocity-divergence-free condition. As the viscous forces and surface forces are always calculated with the constrained particle position and velocity at full time-steps, the velocity-divergence errors introduced by these forces are minimized.

Also, the projection method is extended to multi-phase flow following the approach of Hu and Adams [**?**]. For this new proposed gradient and divergence operators which do not involve the assumption of a differentiable density or viscosity field the density, viscosity and pressure gradient discontinuities are handled naturally. To allow for highly-efficient linear system solvers, such as the preconditioned conjugate gradient method, the Poisson operator is dis-

cretized to result in a symmetric coefficient matrix. It should be emphasized that, as similar approaches are employed to treat density and divergence constraints, the present method introduces only a minor additional complexity compared to previous incompressible SPH methods.

2 Method

We consider the isothermal incompressible Navier-Stokes equations in a moving Lagrangian frame

$$\frac{d\rho}{dt} = 0 \quad \text{or} \quad \nabla \cdot \mathbf{v} = 0 \tag{1}$$

$$\frac{d\mathbf{v}}{dt} = \mathbf{g} - \frac{1}{\rho}\nabla p + \mathbf{F} + \frac{\mathbf{F}^{(1)}}{\rho} \tag{2}$$

where ρ, p, $\mathbf{v}$ and $\mathbf{g}$ are material density, velocity, pressure and body force, respectively. The two expressions (zero density-variation and velocity-divergence free) in Eq. (1) give formally equivalent conditions for an incompressible flow. In the equation of motion Eq. (2), $\mathbf{F}$ denotes the viscous force

$$\mathbf{F} = \nu \nabla^2 \mathbf{v} \tag{3}$$

where $\nu = \eta/\rho$ is the kinematic viscosity. $\mathbf{F}^{(1)}$ denotes the surface force which acts at a phase-interface only. For an immiscible mixture the surface force is given as

$$\mathbf{F}^{(1)} = \nabla \cdot \Pi^{(1)} \tag{4}$$

where the surface stress is

$$\Pi^{(1)} = \alpha \frac{1}{|\nabla C|}\left(\frac{1}{d}\mathbf{I}|\nabla C|^2 - \nabla C \nabla C\right), \tag{5}$$

and α is a surface-tension coefficient, d is the spatial dimension and ∇C is the gradient of a color index C which has a unit jump across the interface.

In Hu & Adams [**?**] the smoothing function for particle i is given by

$$\chi_i(\mathbf{r}) = \frac{W(\mathbf{r} - \mathbf{r}_i, h)}{\sum_k W(\mathbf{r} - \mathbf{r}_k)} = \frac{W_i(\mathbf{r})}{\sigma(\mathbf{r})} \tag{6}$$

where $\mathbf{r}_i$ is the position of particle i, $k = 1, ..., N$. N is the total particle number and h is the smoothing length. $W(\mathbf{r})$ is a generic shape function known as the SPH smoothing kernel. $\sigma(\mathbf{r})$ is a measure of the particle number density which has a larger value in a dense particle region than in a dilute particle region.

We also introduce the volume of a particle through the integral over the entire domain $\mathcal{V}_i = \int \chi_i(\mathbf{r}) d\mathbf{r} \approx \frac{1}{\sigma(\mathbf{r_i})}$ which shows that

$$\sigma_i = \sigma(\mathbf{r_i}) = \sum_j W_{ij}, \tag{7}$$

where $W_{ij} = W(r_{ij}) = W(\mathbf{r}_i - \mathbf{r}_j)$, is approximately the inverse of the particle volume, i.e. the specific volume. The particle density is given by

$$\rho_i = \frac{m_i}{\mathcal{V}_i} = m_i \sigma_i \tag{8}$$

where m_i is mass of particle. Since m_i does not change through the computation in a mass-conservative incompressible SPH formulation, the zero-density-variation condition needs that σ_i is also kept unchanged.

For a smooth variable $\psi(\mathbf{r})$, two forms of discretizations for the particle-averaged spatial derivative are proposed in Hu & Adams [**?**]. The second of these forms is

$$\nabla \psi_i \approx \sigma_i \sum_j \left(\frac{1}{\sigma_i^2} + \frac{1}{\sigma_j^2} \right) \overline{\psi}_{ij} \frac{\partial W}{\partial r_{ij}} \mathbf{e}_{ij} = \sigma_i \sum_j A_{ij} \overline{\psi}_{ij} \mathbf{e}_{ij} \tag{9}$$

where $A_{ij} = \left(\frac{1}{\sigma_i^2} + \frac{1}{\sigma_j^2} \right) \frac{\partial W}{\partial r_{ij}}$, $\frac{\partial W}{\partial r_{ij}} \mathbf{e}_{ij} = \nabla W(\mathbf{r}_i - \mathbf{r}_j)$, and $\frac{\partial W}{\partial r_{ij}} \leq 0$, $\mathbf{r}_i - \mathbf{r}_j = \mathbf{r}_{ij} = r_{ij} \mathbf{e}_{ij}$, and $\mathbf{e}_{ij}$ is the normalized vector pointing from particle i to j. $\overline{\psi}_{ij} = \overline{\psi}(\psi(\mathbf{r}_i), \psi(\mathbf{r}_j))$ is an inter-particle-averaged value. Eq. (9) allows to formulate different inter-particle averages or to assume different inter-particle distributions. For example, a simple inter-particle average is

$$\overline{\psi}_{ij} = \frac{1}{2} [\psi(\mathbf{r}_i) + \psi(\mathbf{r}_j)]. \tag{10}$$

For the particle-averaged second-order spatial derivative one can set $\psi = \nabla \varphi$ to formulate the inter-particle average of the derivative along the direction from particle i to j by

$$\overline{\nabla \varphi_{ij}} = \frac{\mathbf{e}_{ij}}{r_{ij}} \varphi_{ij}, \tag{11}$$

where $\varphi_{ij} = \varphi(\mathbf{r}_i) - \varphi(\mathbf{r}_j)$, and discretize the second-order derivative (Laplacian) directly by

$$\nabla \cdot \nabla \varphi_i \approx \sigma_i \sum_j A_{ij} \frac{\varphi_{ij}}{r_{ij}}. \tag{12}$$

2.1 Projection method

A fractional time-step integration approach is used to solve Eqs. (1) and (2). First, the half-time-step velocity is obtained by

$$\mathbf{v}_i^{n+1/2} = \mathbf{v}_i^n + \left(\mathbf{f} - \frac{1}{\rho}\nabla p\right)_i^n \frac{\Delta t}{2}. \tag{13}$$

Subsequently, the particle position at the new time step is calculated by

$$\mathbf{r}_i^{n+1} = \mathbf{r}_i^n + \mathbf{v}_i^{n+1/2}\Delta t, \tag{14}$$

and the particle velocity at the new time step is obtained by

$$\mathbf{v}_i^{n+1} = \mathbf{v}_i^{n+1/2} + \left(\mathbf{f} - \frac{1}{\rho}\nabla p\right)_i^n \frac{\Delta t}{2}. \tag{15}$$

The two incompressibility conditions in Eq. (1) are enforced simultaneously. The first condition, the zero-density-variation condition, is satisfied by computing the pressure gradient in Eq. (13) to adjust the positions of particles for an unchanged σ_i in Eq. (8). The second condition, the velocity-divergence-free condition, is satisfied by computing the pressure gradients in Eq. (15) to adjust the particle velocity to obtain a divergence-free velocity field.

2.1.1 Zero-density-variation condition

We split Eqs.(13) and (14) into an intermediate step and into a correction step. The intermediate velocity $\mathbf{v}_i^{*,n+1/2}$ and the intermediate particle position $\mathbf{r}_i^{*,n+1}$ are obtained by

$$\mathbf{v}_i^{*,n+1/2} = \mathbf{v}_i^n + \mathbf{f}_i\left(\mathbf{r}^n, \mathbf{v}^n\right)\frac{\Delta t}{2}, \quad \mathbf{r}_i^{*,n+1} = \mathbf{r}_i^n + \mathbf{v}_i^{*,n+1/2}\Delta t, \tag{16}$$

respectively. The intermediate particle density $\rho_i^{*,n+1}$ satisfies

$$\frac{\rho_i^{*,n+1} - \rho_i^n}{\Delta t} + \rho_i^n \nabla_i \cdot \mathbf{v}^{*,n+1/2} = 0. \tag{17}$$

The half-time-step particle velocity $\mathbf{v}_i^{n+1/2}$ is obtained by

$$\mathbf{v}_i^{n+1/2} = \mathbf{v}_i^{*,n+1/2} - \left(\frac{\nabla p}{\rho}\right)_i^n \frac{\Delta t}{2}. \tag{18}$$

From the zero-density-variation condition $\rho_i^{n+1} = \rho_i^n$ and the velocity-divergence-free condition $\nabla_i \cdot \mathbf{v}^{n+1/2} = 0$ one obtains the following relation from Eq. (17)

and (18)

$$\frac{\Delta t^2}{2}\nabla\cdot\left(\frac{\nabla p}{\rho}\right)_i^n = \frac{\rho_i^n - \rho_i^{*,n+1}}{\rho_i^n}, \tag{19}$$

which has a similar form as that in [**?**]. Note that with the relations $\rho_i^n = \rho_i = m_i\sigma_i^0$ and $\rho_i^{*,n+1} = m_i\sigma_i^{*,n+1}$ Eq. (19) can be rewritten to

$$\frac{\Delta t^2}{2}\nabla\cdot\left(\frac{\nabla p}{\rho}\right)_i^n = \frac{\sigma_i^0 - \sigma_i^{*,n+1}}{\sigma_i^0}, \tag{20}$$

in which the right-hand-side equals to the relative error of particle density. At the new time step the particle position $\mathbf{r}^{n+1}$ can be obtained by the correction step

$$\mathbf{r}^{n+1} = \mathbf{r}^{*,n+1} - \left(\frac{\nabla p}{\rho}\right)_i^n \frac{\Delta t^2}{2}. \tag{21}$$

In practice Eqs. (20) and (21) are not solved separately but incorporated into the following iterative scheme

$$\frac{\Delta t^2}{2}\nabla\cdot\left(\frac{\nabla p}{\rho}\right)_i^{n,m-1} \leftarrow \frac{\sigma_i^0 - \sigma_i^{*,n+1,m-1}}{\sigma_i^0} \tag{22a}$$

$$\mathbf{r}^{n+1,m} \leftarrow \mathbf{r}^{n+1,m-1} - \left(\frac{\nabla p}{\rho}\right)_i^{n,m-1} \frac{\Delta t^2}{2} \tag{22b}$$

$$\sigma_i^{*,n+1,m} \leftarrow \mathbf{r}^{n+1,m} \tag{22c}$$

where m is the number of an iteration step and $\sigma_i^{*,n+1,m}$ is obtained from Eq. (7) with updated particle positions.

2.1.2 Velocity-divergence-free condition

An intermediate velocity at the full time step $\mathbf{v}^{*,n+1}$ is obtained by

$$\mathbf{v}_i^{*,n+1} = \mathbf{v}_i^{*,n+1/2} + \mathbf{f}_i\left(\mathbf{r}^n, \mathbf{v}^n\right)\frac{\Delta t}{2}. \tag{23}$$

The velocity at the full time step $\mathbf{v}^{n+1}$ is obtained by

$$\mathbf{v}_i^{n+1} = \mathbf{v}_i^{*,n+1} - \left(\frac{\nabla p}{\rho}\right)_i^n \frac{\Delta t}{2}. \tag{24}$$

To enforce the velocity-divergence-free condition at the new time step, the divergence of Eq. (24) is taken, and by $\nabla_i\cdot\mathbf{v}^{n+1} = 0$ one obtains the required pressure distribution from

$$\frac{\Delta t}{2}\nabla\cdot\left(\frac{\nabla p}{\rho}\right)_i^n = \nabla_i\cdot\mathbf{v}^{*,n+1}. \tag{25}$$

We make the following observations:

- The viscous forces and surface forces are always calculated by Eq. (23) at the corrected full time step particle position and velocity, the divergence errors introduced by the discretizations of these forces are therefore minimized.
- In practice, the density correction of Eq. (22) is only performed at those time steps for which the maximum density error for at least one particle is larger than a certain threshold. As the density errors after a single time step are small, the density correction usually is rarely invoked and the increase of computational expenses is rather low. Typically, the number of iteration decreases if larger density error is permitted, or if the particle resolution is carried increased. Our experience suggests that the iteration count is less than $\mathcal{O}(10)$ if the permitted maximum density error is 1% or 0.5%.
- As shown in the next section, the discretization operators and linear-system solvers involved in enforcing the density and velocity constraints, Eqs. (20) and (25), are the same. The use of a density constraint in addition to the velocity constraint introduces only a minor coding overhead as compared to previous approaches.

2.1.3 A multi-phase projection formulation

Since velocity, pressure and viscous forces are continuous even for a discontinuous density $\frac{\nabla p}{\rho}$ has to be continuous owning to Eqs. (20) and (25). If ρ is discontinuous ∇p is also discontinuous. For a single-phase incompressible flow with density ρ the inter-particle-averaged directional derivative $\overline{\left(\frac{\nabla p}{\rho}\right)}_{ij}$ is approximated by Eq. (11) as

$$\overline{\left(\frac{\nabla p}{\rho}\right)}_{ij} = \frac{p_{ij}}{\rho r_{ij}}\mathbf{e}_{ij} \tag{26}$$

where $p_{ij} = p_i - p_j$. If particle i and j belong to different phases with a density discontinuity one can assume that the phase interface is located at the center m between particle i and j, and that the discontinuity is on a plane normal to the inter-particle vector $\mathbf{r}_{ij}$. To ensure the continuity of $\overline{\left(\frac{\nabla p}{\rho}\right)}_{ij}$ and of the pressure across the interface we require

$$\frac{p_{im}}{\rho_i r_{im}}\mathbf{e}_{im} = \frac{p_{mj}}{\rho_j r_{mj}}\mathbf{e}_{mj} \tag{27}$$

where $r_{im} = r_{mj} = \frac{1}{2}r_{ij}$, $\mathbf{e}_{im} = \mathbf{e}_{mj} = \mathbf{e}_{ij}$. Note that $p_{ij} = p_{im} + p_{mj}$ the inter-particle-averaged $\overline{\left(\frac{\nabla p}{\rho}\right)}_{ij}$ at the phase interface is

$$\overline{\left(\frac{\nabla p}{\rho}\right)}_{ij} = \frac{2}{r_{ij}}\frac{p_{ij}}{\rho_i + \rho_j}\mathbf{e}_{ij}, \tag{28}$$

which gives the inter-particle pressure

$$p_m = \frac{\rho_i p_j + \rho_j p_i}{\rho_i + \rho_j}. \tag{29}$$

According to Eq. (12) the Poisson operators in Eqs. (20) and (25) can be discretized as

$$\nabla \cdot \left(\frac{\nabla p}{\rho} \right)_i = 2\sigma_i \sum_j \frac{A_{ij}}{r_{ij}} \frac{p_{ij}}{\rho_i + \rho_j}. \tag{30}$$

The resulting discretization for Eq. (20) can be written as

$$\sum_j \frac{A_{ij}}{r_{ij}} \frac{p_{ij}}{\rho_i + \rho_j} = \frac{1}{2} \frac{\sigma_i^0 - \sigma_i^*}{\sigma_i^0 \sigma_i^*}. \tag{31}$$

The right-hand side of Eq. (25) is discretized as

$$\nabla_i \cdot \mathbf{v}^* = \sigma_i \sum_j A_{ij} \overline{\mathbf{v}_{ij}^*} \cdot \mathbf{e}_{ij}. \tag{32}$$

For single-phase flow one can define the inter-particle average velocity $\overline{\mathbf{v}_{ij}^*}$ by Eq. (10). If particle i and j belong to different phases with a viscosity discontinuity, the inter-particle-averaged velocity is given by

$$\mathbf{v}_m = \frac{\eta_i \mathbf{v}_i + \eta_j \mathbf{v}_j}{\eta_i + \eta_j}, \tag{33}$$

in which η_i and η_j are viscosities for the two particles, to ensure continuity of the viscous force [**?**]. Hence, the resulting discretization for Eq. (25) can be written as

$$\sum_j \frac{A_{ij}}{r_{ij}} \frac{p_{ij}}{\rho_i + \rho_j} = \frac{1}{2} \sum_j A_{ij} \left(\frac{\eta_i \mathbf{v}_i + \eta_j \mathbf{v}_j}{\eta_i + \eta_j} \right) \cdot \mathbf{e}_{ij}. \tag{34}$$

According to Eq. (**??**), one can discretize the pressure gradient as

$$\left(\frac{\nabla p}{\rho} \right)_i = \frac{1}{m_i} \sum_j A_{ij} \frac{\rho_i p_j + \rho_j p_i}{\rho_i + \rho_j} \mathbf{e}_{ij}. \tag{35}$$

Note that the left-hand-side of Eqs. (**??**) and (**??**) have the same expressions and define a symmetric linear system for periodic or von Neumann boundary conditions [**?**]. Therefore, highly-efficient solvers, such as the preconditioned conjugate gradient method, can be implemented in a straightforward way. In Cummins & Rudman [**?**] and Shao & Lo [**?**] the projection operator is symmetric for single-phase flows but not for flows with variable density. Note that, as the projection operator involves all neighboring particles (for example about 21 particles for a quartic spline smoothing kernel and about 29 particles for a quintic spline smoothing kernel) in the SPH method, the band width of the coefficient matrix is much wider than that of a moderate-order finite

difference method. Therefore, the same elliptic solver requires considerably more operations for an SPH method than for such a finite difference method.

2.1.4 Reference pressure

When Eqs. (**??**) and (**??**) are solved with zero initial values under a von Neumann boundary condition negative pressure may occur in some region of the computational domain. It is well known that a negative pressure may cause stability problems in SPH. To overcome this difficulty a constant positive reference pressure is superimposed onto the computed pressure. Following Morris et al. [**?**] and Hu & Adams [**?**], a physically reasonable reference pressure p_{ref} can be estimated by considering the balance of forces in the equation of motion (2). Given a velocity scale V_0 and length scale L_0, the terms on the right-hand side should be of comparable magnitude, that is

$$\frac{p_{ref}}{\rho_{max}} \sim V_0^2 \sim \frac{\nu_{max} V_0}{L_0} \sim g L_0 \sim \max\left(\frac{\alpha^{kl}\kappa_c^{kl}}{\min(\rho_k, \rho_l)}\right), \quad k \neq l \tag{36}$$

where ρ_{max} and ν_{max} are the maximum density and kinematic viscosity, respectively. α^{kl} and κ_c^{kl} are surface tension and typical curvature between phase k and l, respectively. After a simulation has been run initially at low resolution and the actual variation in pressure is known, the value of p_{ref} can be changed to ensure a positive pressure p. As the conservative discretization of pressure gradient, Eq. (9), in SPH method produces residual fluctuation even for constant pressure, the introduction of a reference pressure leads to small fluctuations proportional to the reference pressure magnitude. Therefore, one should choose p_{ref} as small as possible for better accuracy.

2.2 Time step criteria

For stability several time-step criteria [**?**] must be satisfied, including a CFL condition

$$\Delta t \leq 0.25 \frac{h}{|U|_{max}}, \tag{37}$$

where $|U|_{max}$ is the maximum velocity in the flow, a viscous-diffusion condition

$$\Delta t \leq 0.25 \frac{h^2}{\nu_{max}}, \tag{38}$$

where ν_{max} are the maximum kinematic viscosity, and surface tension condition [**?**] [**?**]

$$\Delta t \leq 0.25 \min\left(\frac{\min(\rho_k, \rho_l) h^3}{2\pi\alpha^{kl}}\right)^{1/2}, \quad k \neq l. \tag{39}$$

As the CFL time-step condition for weakly compressible SPH is

$$\Delta t \leq 0.25 \frac{h}{c_{max} + |U|_{max}} \tag{40}$$

where $c_{max} \geq 10|U|_{max}$ is the maximum artificial sound speed, it is computationally less efficient than the incompressible SPH when the flow evolution is not dominated by the viscous force or the surface tension. If the flow is viscosity or surface-tension dominanted, the efficiency of incompressible SPH can be further increased by a multi-time step technique, in which the viscous force and the surface tension calculated, by Eqs. (16) and (23), are updated with time steps according to conditions (**??**) and (**??**) whereas the pressure projection is performed with time steps according to condition (**??**).

As the error introduced by the reference pressure may cause a stability problem, in the present method also a global time step criterion needs to be introduced

$$\Delta t \leq 0.25 \frac{h}{c_{ref} + |U|_{max}}, \tag{41}$$

where c_{ref} is the artificial reference sound speed defined by $p_{ref} = \rho_{min} c_{ref}^2$. From Eqs. (**??**) and (**??**), it can be found that for a single-phase flow or flows with moderate density ratios c_{ref} is of the order of $|U|_{max}$. Then the new time step criterion only slightly decreases the time step size. However, for large density ratios the time step limit by Eq. (**??**) is dominant. Whenever the resulting time step size is close to that of a weakly compressible SPH method, the incompressible SPH is computationally less efficient since enforcing the incompressible conditions causes computational overhead.

3 Numerical examples

The following two-dimensional numerical examples are provided to validate the proposed incompressible multi-phase SPH method. For all cases a quintic spline kernel [**?**] is used. A constant smoothing length, which is kept equal to the initial distance between the neighboring particles, is used for all the test cases. As elliptic solver a diagonal or SSOR preconditioned conjugate gradient method is used. If not mentioned otherwise, the permitted maximum density error is 1%, and no-slip wall boundary conditions are implemented following the approach of Cummins & Rudman [**?**].

3.1 Two-dimensional Taylor-Green flow

The two-dimensional viscous Taylor-Green flow is a periodic array of vortices, where the velocity

$$\begin{aligned} u(x,y,t) &= -Ue^{bt}\cos(2\pi x)\sin(2\pi y) \\ v(x,y,t) &= \ Ue^{bt}\sin(2\pi x)\cos(2\pi y) \end{aligned} \tag{42}$$

is an exact solution of the incompressible Navier-Stokes equation. $b = -\frac{8\pi^2}{\mathrm{Re}}$ is the decay rate of velocity field. We consider a case with $\mathrm{Re} = 100$. The computation is performed on a domain $0 < x < 1$ and $0 < y < 1$ with periodic boundary conditions in both directions. The initial particle velocity is assigned according to Eq. (**??**) by setting $t = 0$ and $U = 1$. In order to study the convergence properties the calculation is carried out with 900, 3600, 14400 particles, respectively. Two initial particle configurations are considered: one is starting from regular lattice positions; the other is starting from previously stored particle position (relaxed configuration). The following discussion is based on results calculated from the latter, while the results calculated from lattice configurations are used to study the influence of initial particle position.

Figure **??** shows calculated positions of particles and vorticity profile, respectively, at $t = 1$ with 3600 particles. It can be observed that a uniform particle distribution without clustering is produced. The current SPH simulation recovers the theoretical solution quite well with somewhat larger errors in regions close to the centers of vortex cells. Figure **??**a shows the evolution of the maximum velocity of the flow calculated with 900 particles. Compared to the analytical solution the current method predicts the decay process very accurately. When the same case is run from an initial lattice configuration the predicted decay rate is slight larger (see Fig. **??**a for the line denoted as A). However, for both cases the difference to the analytical solution is small. At time $t = T_{max}$, where $U_{max}^{T_{max}} = \frac{U}{50}$, the relative error $\left|\frac{U_{max}^{ex} - U_{max}^{SPH}}{U_{max}^{ex}}\right|$, where U_{max}^{ex} denotes the maximum velocity of the exact solution and U_{max}^{SPH} that of the simulation, reaches at most 2% which is even smaller than the 4% obtained by starting from a relaxed particle configuration. Note that with only about 1/10 the number of particles the accuracy of the current simulation is comparable with that of the re-meshing SPH method [**?**] (see their Fig. 3), in which the errors caused by particle disorder are reduced by re-sampling the SPH particles at every time step.

If the particle density is not constrained with Eq. (22), as shown in Fig. **??**a (the line denoted as B) the error increases considerably. Furthermore, if the particle density is not constrained and the computation starts from a lattice configuration, the errors increase further (see Fig. **??**a for the line denoted as

C). Another difficulty encountered for an unconstrained solution is that the density error may accumulate if a strong vortical flow evolves in the solution [**?**]. As shown in Fig. **??**b, the unconstrained solution has a relative density error close to 4% while the error is 1% for the constrained solution. On the other hand, the relative density error for the unconstrained solution apparently strongly depends on the initial particle configuration. As shown in Fig. **??**b, the relative errors can reach more than 20% when starting from the lattice configuration.

For convergence analysis, we calculate the relative error of the computed maximum velocity up to time T_{max} shown in Fig. **??**a for the solution with 900, 3600 and 14400 particles. The L_∞ errors are obtained by

$$L_\infty = \max\left(\left|\frac{U_{max}^{ex} - U_{max}^{SPH}}{U_{max}^{ex}}\right|\right). \tag{43}$$

It is found that the convergence rate of the L_∞ error is about first order. The calculated velocity profiles in x direction at two positions, $y = 0.3$ and $y = 0.5$, with different resolutions are shown in Fig. **??** which indicate an about first order convergence rate for the peak velocities.

3.2 Capillary wave

We consider two problems of liquid-droplet oscillation under the action of capillary forces. The first problem, taken from Morris [**?**] and Hu & Adams [**?**], is a droplet oscillating in a liquid phase with the same density. The second problem, taken from Wu et al. [**?**], is a droplet oscillating in a liquid environment with different density.

For the first problem, the computation is performed on a domain $0 < x < 1$ and $0 < y < 1$ using fluids of the same density $\rho_d = \rho_l = 1$ and equal viscosity $\eta = 0.05$. A droplet of radius $R = 0.1875$ is placed at the domain center and the surface-tension coefficient is $\alpha = 1$. To all particles a divergence-free initial velocity $v_x = V_0\frac{x}{r_0}(1 - \frac{y^2}{r_0 r})\exp(-\frac{r}{r_0})$ and $v_y = V_0\frac{y}{r_0}(1 - \frac{x^2}{r_0 r})\exp(-\frac{r}{r_0})$ is assigned, where $V_0 = 10$, $r_0 = 0.05$, and r is the distance from the position (x, y) to the droplet center. In order to study the convergence properties the calculation is carried out with 900, 3600, 14400 particles, respectively.

Figure **??** shows the positions of the droplet particles at 4 selected time instants with 14400 particles. It is observed that particle distribution is in quite good agreement with the results of Hu & Adams [**?**] (their Fig. 4). Figure **??** compares the variation of the center-of-mass position and velocity of the upper left 1/4 part of the droplet with different resolutions. The computed first period at the highest resolution is about 0.35. Compared with the results in

Hu & Adams [**?**], we find that while the computed periods differ by only 3% the noise caused by artificial sound waves in the weakly compressible SPH is eliminated by the present method. First order convergence rates are obtained for both mass center position and velocity by calculating the relative error between different resolutions. Again, the accuracy is quite close that of weakly compressible SPH [**?**] while numerical artifacts are removed.

For the second problem, the computation is performed on a domain $0 < x < 12$ and $0 < y < 8$, and an elliptic droplet defined by $x^2/4 + y^2 = 1$ is placed at the domain center and the surface-tension coefficient is $\alpha = 1$. The densities inside and outside of the drop are 1.5 and 0.5, respectively, and the viscosity is 1×10^{-2}. Initially, the particle velocity is set to zero. The problem is simulated with 3456 particles.

Figure **??** shows the positions of the droplet particles at 4 selected time instants. It is observed that the interface deformation is in quite good agreement with the results of Wu et al. [**?**] obtained by a higher resolution finite-element calculation (their Fig. 4). The corresponding time history of the center-of-mass position in x direction of the upper left 1/4 part and the total kinetic energy of the drop are shown in Fig. **??**. The oscillation period is estimated (based on the first two cycles) to be 7.38 which is, again, close to the result of 7.6 in Wu et al. [**?**].

3.3 Drop deformation in shear flow

We consider a circular drop with initial radius $R_o = 0.02$ in a Couette flow with top and bottom wall velocity of $\pm v$, respectively. The periodic computational domain is the region $0 < x < 8R_o$ and $0 < y < 8R_o$ in which the drop is centered at $(4R_o, 4R_o)$. The calculation is carried out with 9216 particles. The drop deforms with the flow until a balance between viscous stresses and surface tension is reached. It is known that the shape of sheared drop is governed by two nondimensional parameters, i.e. the viscosity ratio $\lambda = \eta_d/\eta_c$, where η_d and η_c are, respectively, the viscosities of the drop and the shearing fluid, and the capillary number $\mathrm{Ca} = 0.25\eta_d v/\alpha$. According to [**?**], a linear deformation is predicted theoretically under the condition of small capillary number, and the deformation parameter is given by

$$D = \mathrm{Ca}\frac{19\lambda + 16}{16\lambda + 16} \tag{44}$$

in which $D = (L - B)/(L + B)$, L and B are the drop's half-length and half-width, respectively.

Figure **??**a shows the final equilibrium stage when $\mathrm{Ca} = 0.15$ and $\lambda = 1$. Note

that the shape of the deformed drop agrees with the weakly SPH simulation result [**?**] quite well while the present method produces a notably uniform particle distribution. The measured D is about 0.153 which is close to the result obtained by Zhou & Pozrikidis [**?**] and Hu & Adams [**?**]. Figure **??**b shows a comparison of the results of [**?**][**?**] and the current computations for several capillary numbers. To study the dependence on the viscosity ratio, we simulate the drop deformation for $\mathrm{Ca} = 0.15$ with different viscosity ratios, ranging from $\lambda = 0.01$ to 100. In Fig. **??**a can be seen that the drop deformation increases with λ. Note that predicted deformation variations are less than that obtained from [**?**]. The present results are in accordance with the theoretical prediction by Eq. (**??**) which implies that D only increases slightly with λ. The drop deformation in the non-linear regime is also examined. Figure **??**b shows the deformed drop for $\mathrm{Ca} = 1.5$ and $\mathrm{Re} = 0.25\rho R_0 v/\eta_c = 3$. The drop does not break up even after being stretched to form a strip with the length about twice that of the domain width. Note that the strip center is thicker than the two necks, which is in agreement with the three-lobed mode for drop deformation under conditions of large capillary number but small Reynolds number [**?**].

3.4 Rayleigh-Taylor instability

We consider a Rayleigh-Taylor instability problem which has been studied by Cummins & Rudman [**?**] with three different methods: finite differences, weakly compressible SPH and incompressible SPH. The computation is performed on a domain $0 < x < 1$ and $0 < y < 2$. Initially, the particles are placed on regular lattice positions. In the lower part of the domain are particles with density $\rho_l = 1.0$. In the upper domain, defined by $y > 1 - 0.15\sin(2\pi x)$, are particles with density $\rho_u = 1.8$. The Reynolds number is set to $\mathrm{Re} = 420$ and the Froude number is set to $\mathrm{Fr} = 1$. No surface tension is included. The initial particle velocity is set to zero, and the permitted maximum density error is 0.5%. The calculation is carried out with 7200 particles, which is a similar resolution as that in [**?**].

The calculated positions of particles at time $t = 1$, $t = 3$ and $t = 5$ are shown in Fig. **??**. Note that the interface evolves into an asymmetric shape because the spike falls (heavy into light fluid) faster than the bubble rises (light into heavy fluid). The general features shows a good agreement with the results in [**?**] (see their Figs. 10 and 11). However, the present results predict a much stronger roll-up of the plumes than their results obtained by incompressible SPH and weakly compressible SPH (comparing the present Fig. **??**b, c to their Figs. 10b, c and Figs. 11b, c). It is quite interesting that the present results indicate even slightly stronger roll-up than that obtained by the finite-difference simulation at similar resolution (comparing to their Figs. 10a and 11a). According to

Hoover [**?**], this may be expected since the present method treats density discontinuities directly, and furthermore the non-smeared density discontinuity strongly increases the baroclinic vorticity production and hence introduces a considerably larger roll-up effect. Compared to finite difference methods which also smoothen the density discontinuities within a narrow band of several grid points, the present SPH algorithm represents the interface in an even sharper way by recovering an exact discontinuity. Another important property of the present results is that there is no noticeable "particle clumping" problem (see Fig. 13 in [**?**]), in which the spurious pressure (artificial surface tension) prevents the formation of high curvature and produces a gap at the interface [**?**]. These interface properties of the present method imply a considerably smaller interface dissipation which explains the quickly developing secondary instabilities as shown in Fig. **??**c.

4 Concluding remarks

We have developed an incompressible multi-phase SPH method in which both the zero-density-variation and velocity-divergence-free constraints of the incompressiblility condition are enforced by a fractional time-step integration algorithm. A new multi-phase projection formulation in which the gradient and divergence operators are not restricted to a differentiable density and viscosity field is developed to obtain non-smeared density and viscosity discontinities. Numerical examples are investigated and compared with analytic solutions and previous results. The results show that the method can be reliably applied to incompressible single-phase and multi-phase flows within and beyond the low Reynolds number region. In addition, since very similar approaches are employed to treat density and divergence constraints, the present method increases coding complexity only slightly.

References

[1] O. Agertz, B. Moore, J. Stadel, D. Potter, F. Miniati, J. Read, L. Mayer, A. Gawryszczak, A. Kravtsov, J. Monaghan, Å. Nordlund, F. Pearce, V. Quilis, D. Rudd, V. Springel, J. Stone, E. Tasker, R. Teyssier, J. Wadsley, and R. Walder. Fundamental differences between sph and grid methods. *arXiv:astro-ph/0610051*, 2006.

[2] J. U. Brackbill, D. B. Kothe, and C. Zemach. A continuum method for modeling surface tension. *J. Comput. Phys.*, 100:335, 1992.

[3] A. K. Chaniotis, D. Poulikakos, and P. Koumoutsakos. Remeshed smoothed particle hydrodynamics for the simulation of viscous and heat conducting flows.

J. Comput. Phys., 182:67, 2002.

[4] S. J. Cummins and M. Rudman. An sph projection method. *J. Compu. Phys.*, 152:584, 1999.

[5] M. Ellero, M. Serrano, and P. Espa nol. Incompressible smoothed particle hydrodynamics. *J. Phys. Comput.*, accepted, 2006.

[6] R. A. Gingold and J. J. Monaghan. Smoothed particle hydrodynamics - theory and application to non-spherical stars. *Mon. Not. R. Astron. Soc.*, 181:375, 1977.

[7] Wm. G. Hoover. Isomorphism linking smooth particles and embeded atoms. *Physica A*, 260:244, 1998.

[8] X. Y. Hu and N. A. Adams. A multi-phase sph method for macroscopic and mesoscopic flows. *J. Comput. Phys.*, 213:844, 2006.

[9] L. B. Lucy. A numerical approach to the testing of the fission hypothesis. *Astron. J.*, 82:1013, 1977.

[10] Y. Meleán, L. Di G. Sigalotti, and A. Hasmy. On the sph tensile instability in forming viscous liquid drops. *Comput. Phys. Commun.*, 157:191, 2004.

[11] J.J. Monaghan. Smoothed particle hydrodynamics. *Ann. Rev. Astronom. Astrophys.*, 30:543, 1992.

[12] J.J. Monaghan. Simulating free surface flows with sph. *J. Comput. Phys.*, 110:399, 1994.

[13] J.J. Monaghan. Smoothed particle hydrodynamics. *Rep. Prog. Phys.*, 68:1703, 2005.

[14] J. P. Morris. Simulating surface tension with smoothed particle hydrodynamics. *Int. J. Numer. Meth. Fluids*, 33:333, 1999.

[15] J. P. Morris, P. J. Fox, and Y. Zhu. Modeling low reynolds number incompressible flows using sph. *J. Comput. Phys.*, 136:214, 1997.

[16] J. Pozorski and A. Wawreńczuk. Sph computation of incompressible viscous flows. *J. Theo. App. Mech.*, 40:917, 2002.

[17] S. Shao and E. Y. M. Lo. Incompressible sph method for simulating newtonian and non-newtonian flows with a free surface. *Advances in Water Resources*, 26:787, 2003.

[18] L. Di G. Sigalotti, J. Klapp, E. Sira, Yasmin Meleán, and A. Hasmy. SPH simulations of time-dependent poiseuille flow at low reynolds numbers. *J. Comput. Phys.*, 191:622, 2003.

[19] G. I. Taylor. The formation of emulsions in definable fields of flows. *Proc. R. Soc. Lond. A*, 146:501, 1934.

[20] A. J. Wagner, L. M. Wilson, and M. E. Cates. Role of inertia in two-dimensional deformation and breakdown of a droplet. *Phys. Rev. E*, 68:045301, 2003.

[21] J. Wu, S. T. Yu, and B. N. Jiang. Simulation of two-fluid flows by the least-square finite element method using a continuum surface tension model. *Int. J. Numer. Meth. Engng.*, 42:583, 1998.

[22] H. Zhou and C. Pozrikidis. The flow of suspensions in channels: Single files of drops. *Phys. Fluids A*, 5:311, 1993.

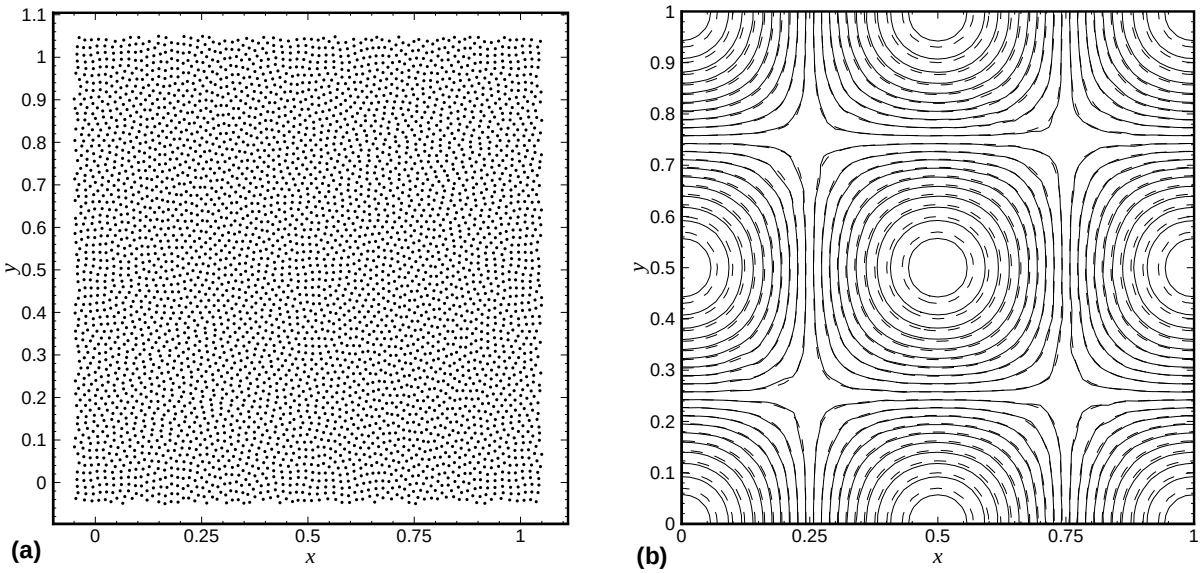

Fig. 1. Taylor-Green problem at $t = 1$ with 3600 particles: (a) positions of particles, (b) simulated vorticity profile (solid line) and analytical solution (dash line)

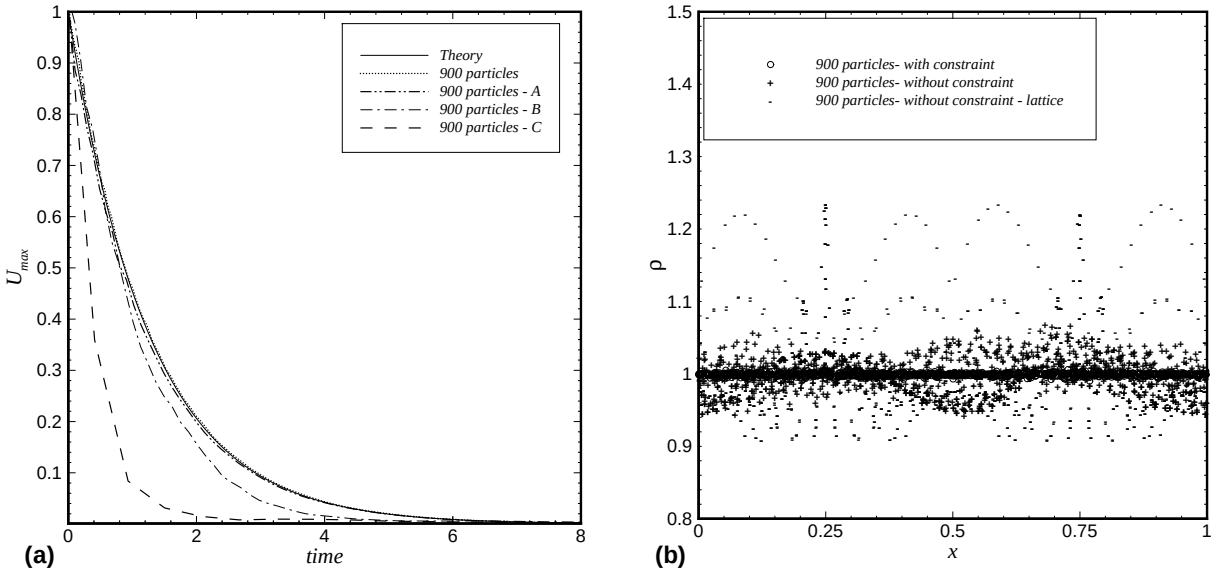

Fig. 2. Taylor-Green problem with 900 particles: (a) decay of the maximum velocity, (b) particle density profile at $t = 1$.

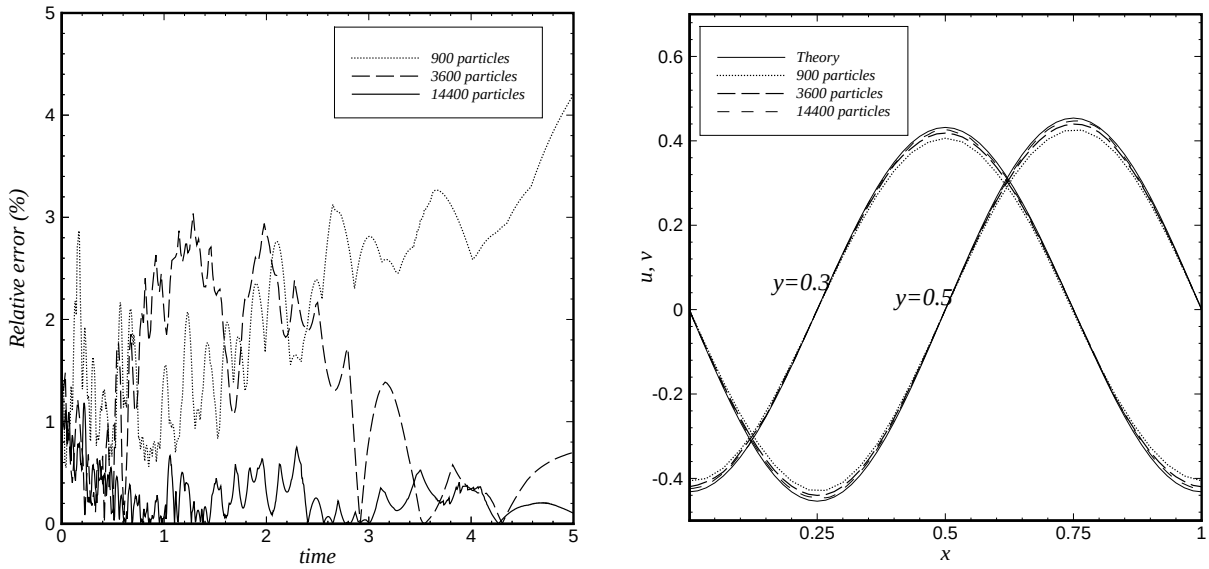

Fig. 3. Taylor-Green problem: SPH solution with different resolutions, (a) relative errors for maximum velocity, (b) velocity profiles u at $y = 0.3$ and v at $y = 0.5$.

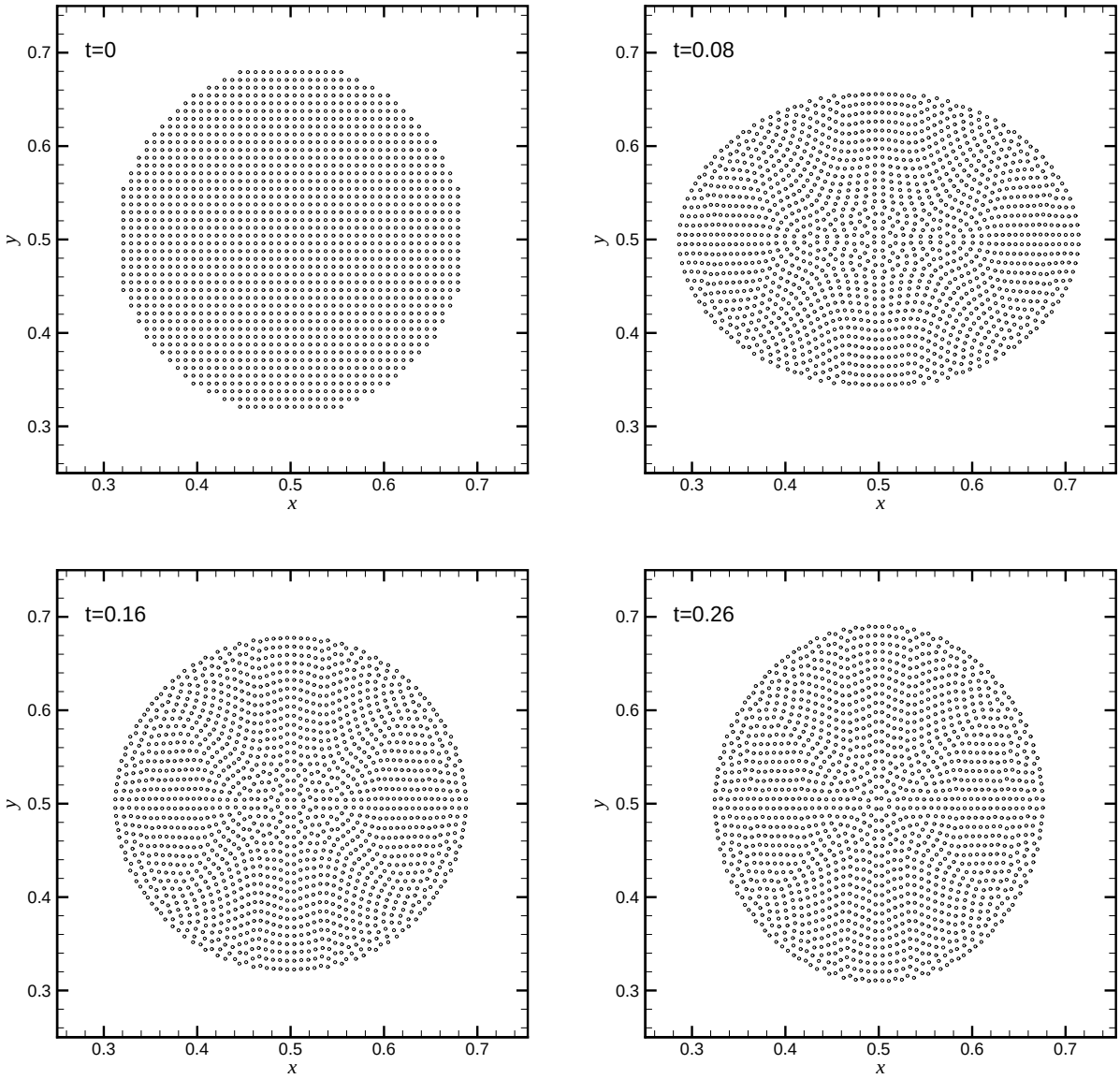

Fig. 4. Droplet oscillation with $\rho_d/\rho_l = 1$: positions of particles at $t = 0$, $t = 0.08$, $t = 0.16$ and $t = 0.26$.

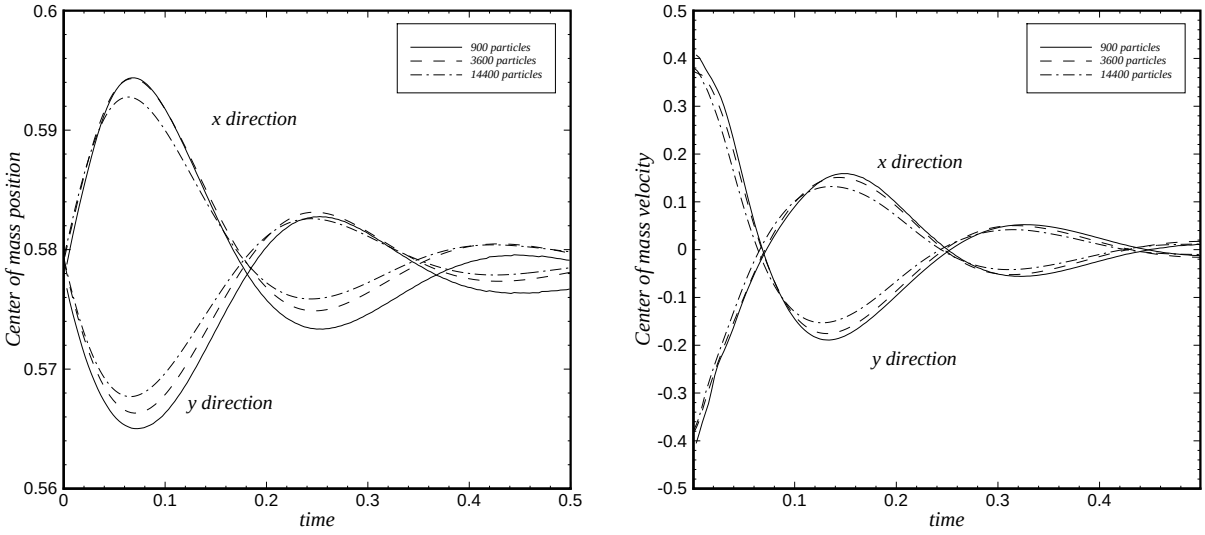

Fig. 5. Droplet oscillation with $\rho_d/\rho_l = 1$: convergence test.

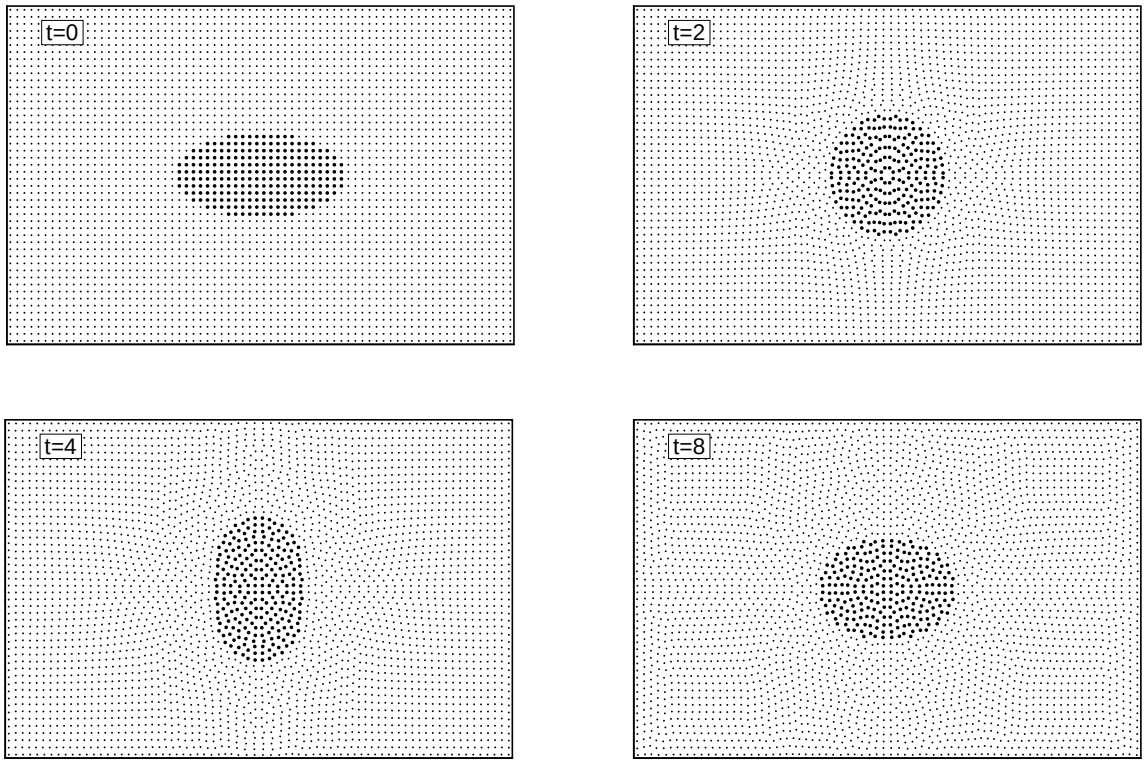

Fig. 6. Droplet oscillation with $\rho_d/\rho_l = 3$: positions of particles at 4 selected time instants.

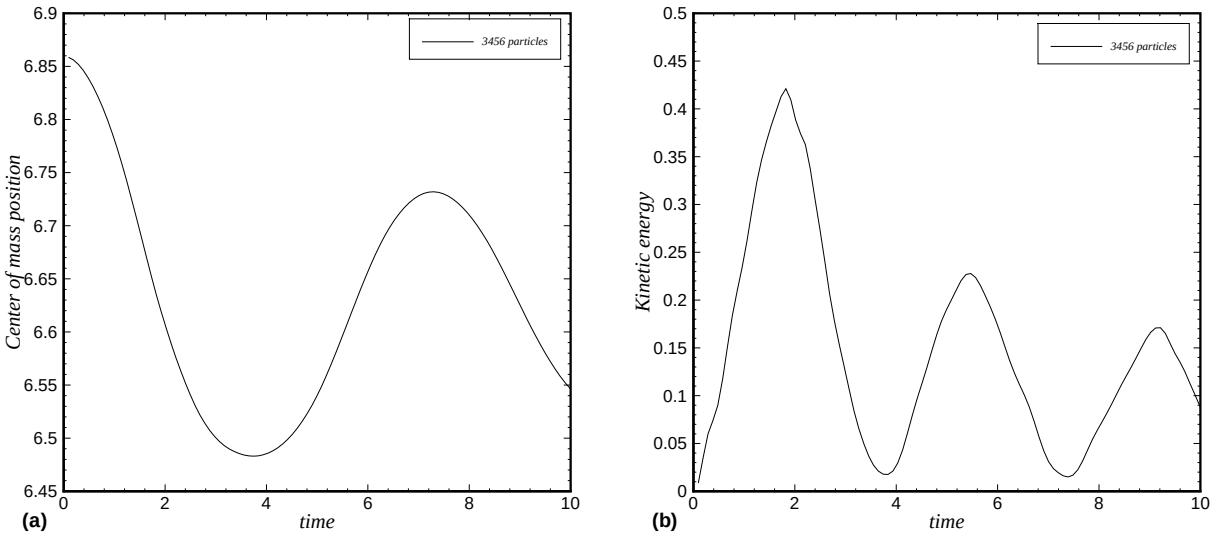

Fig. 7. Droplet oscillation with $\rho_d/\rho_l = 3$: (a) mass center position, in x direction, of the upper left 1/4 part; (b) total kinetic energy of the drop.

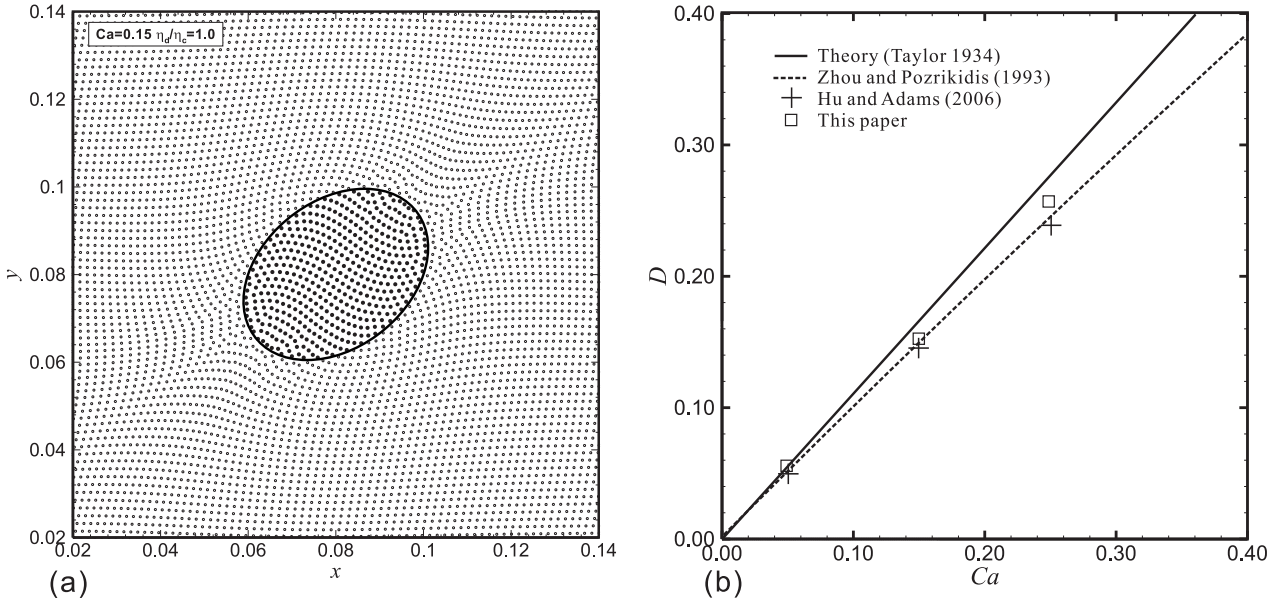

Fig. 8. Drop deformation in a shear flow: (a) particle positions of the drop (black dots) and the shearing fluid (open circles) when Ca = 0.15 and $\lambda = 1$, (b) relation between the deformation parameter and capillary number.

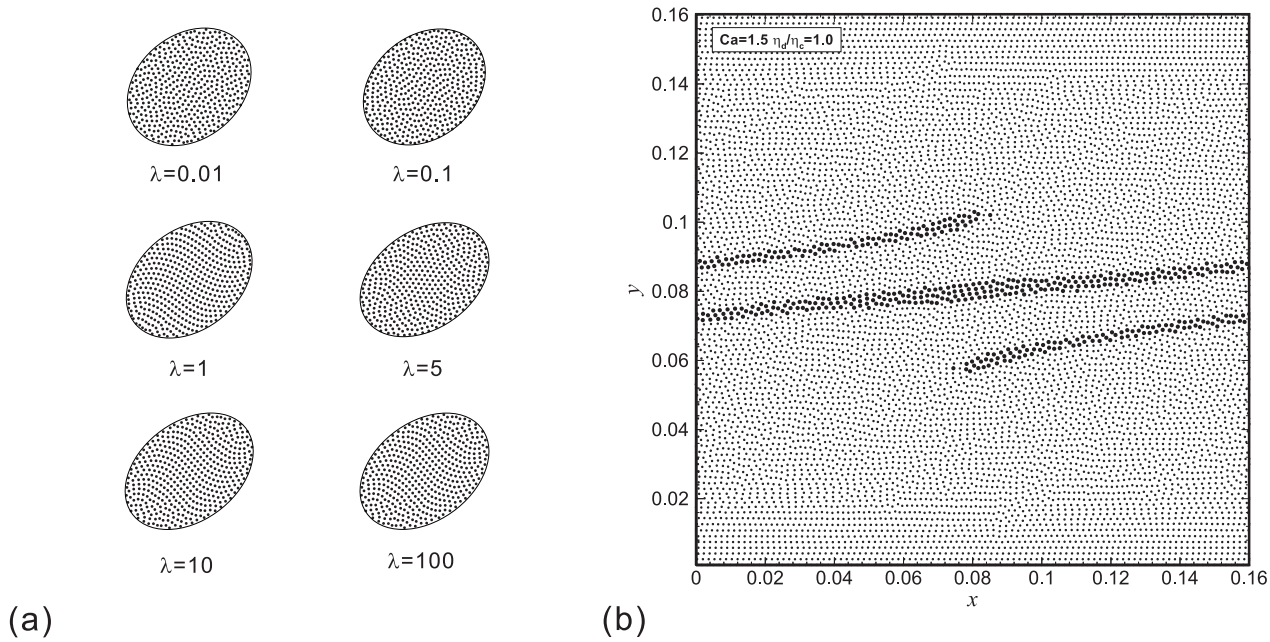

Fig. 9. Drop deformation in a shear flow: (a) drop deformation with different viscosity ratios, (b) deformation of drop with Ca = 1.5 and Re = 3.

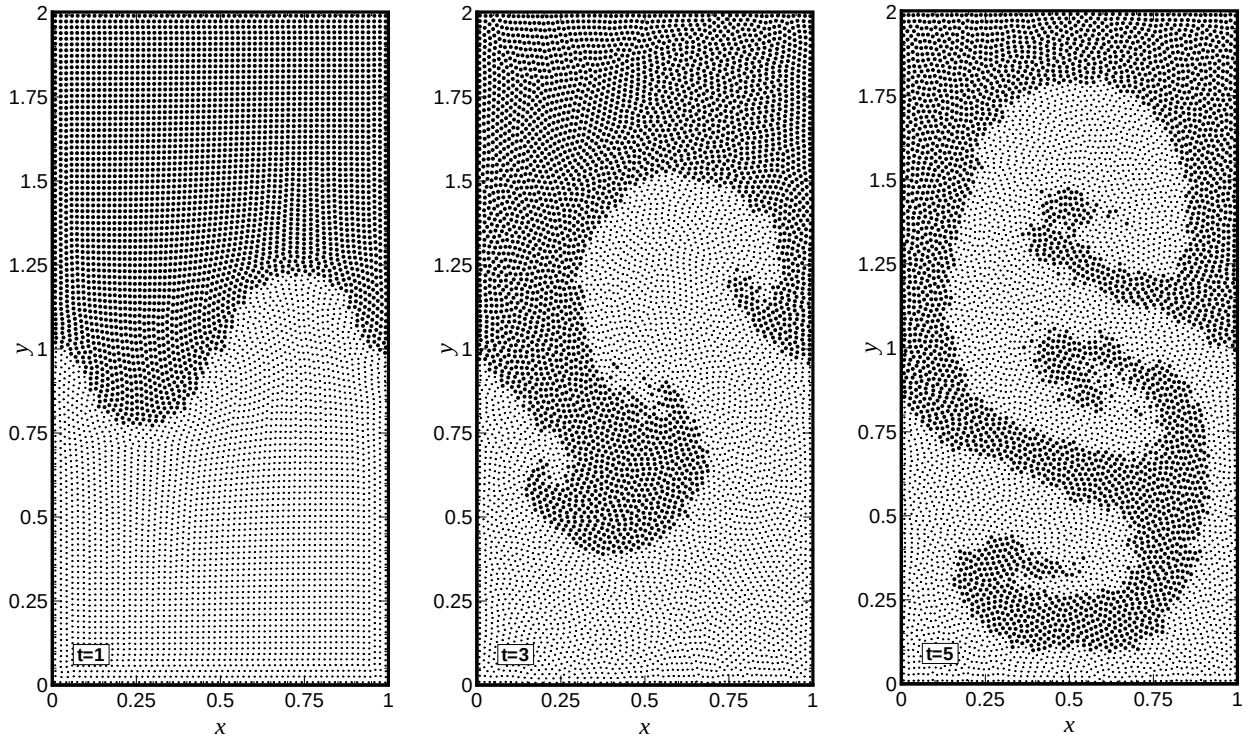

Fig. 10. Rayleigh-Taylor instability: position of particles at 3 selected time instants.